

Molecular dynamics simulation of Al grain mixing in Fe/Ni matrices and its influence on oxidation

O. Verners, Y. K. Shin, and A. C. T. van Duin

Citation: *Journal of Applied Physics* **114**, 023501 (2013); doi: 10.1063/1.4812387

View online: <http://dx.doi.org/10.1063/1.4812387>

View Table of Contents: <http://scitation.aip.org/content/aip/journal/jap/114/2?ver=pdfcov>

Published by the [AIP Publishing](#)

Articles you may be interested in

[Engineering of high performance supercapacitor electrode based on Fe-Ni/Fe₂O₃-NiO core/shell hybrid nanostructures](#)

J. Appl. Phys. **117**, 105101 (2015); 10.1063/1.4913218

[Effect of grain size on superelasticity in Fe-Mn-Al-Ni shape memory alloy wire](#)

APL Mater. **1**, 032103 (2013); 10.1063/1.4820429

[Relation between glass and quasicrystal formation in the Zr–Nb–Cu–Ni–Al alloys upon solidification](#)

Appl. Phys. Lett. **97**, 031919 (2010); 10.1063/1.3467827

[Effect of buffer layer on antiferromagnetic grain size and exchange-coupling field of Cr 70 Al 30 /Fe 19 Ni 81 bilayers](#)

J. Appl. Phys. **83**, 7213 (1998); 10.1063/1.367822

[Effect of antiferromagnetic grain size on exchange-coupling field of Cr 70 Al 30 /Fe 19 Ni 81 bilayers](#)

Appl. Phys. Lett. **71**, 1258 (1997); 10.1063/1.119866



SHIMADZU Powerful, Multi-functional UV-Vis-NIR and FTIR Spectrophotometers

Excellence in Science

Providing the utmost in sensitivity, accuracy and resolution for applications in materials characterization and nano research

- Photovoltaics
- Polymers
- Thin films
- Paints
- Ceramics
- DNA film structures
- Coatings
- Packaging materials

[Click here to learn more](#)



Molecular dynamics simulation of Al grain mixing in Fe/Ni matrices and its influence on oxidation

O. Verners, Y. K. Shin, and A. C. T. van Duin

*Department of Mechanical and Nuclear Engineering, Pennsylvania State University,
136 Research East Building, University Park, Pennsylvania 16802, USA*

(Received 18 April 2013; accepted 11 June 2013; published online 8 July 2013)

$\text{Al}_x\text{Ni}_y\text{Fe}_{(1-x-y)}$ alloys are structural materials with potential application in high-temperature oxidizing environments. These materials are of specific interest as they have the ability to develop an oxidation resistant surface layer. To study diffusion and oxidation processes related to this surface layer formation, the mixing behavior of different sized Al grains in pure Ni and Fe matrices, with approximate grain/matrix atom ratio of 1:3, at temperatures above and below the structure melting point, was studied using ReaxFF-based molecular dynamics simulations. The simulations have been carried out at constant pressure, with temperatures being stepwise ramped over the range of 300–3000 K. For the Ni matrix, our results indicated lower chemical strain energy for Al in the mixed alloy and completion of mixing at a lower temperature for the Fe matrix. These results confirm that the Al-Ni alloy is energetically more stable than the Al-Fe alloy, which is in agreement with experiment. Further, larger Al grains appear to be favorable for mixing with Fe matrix, whereas for Ni matrix, smaller Al grains appear to be favorable. We suggest that this Al grain size effect on mixing matrices is due to the differences in formation energies between Ni/Al and Fe/Al alloys and differences in Ni-Ni and Fe-Fe bond distances. We also performed additional cooling simulations over the temperature range of 3000–300 K. The simulations revealed that for the considered cooling rate Fe alloy solidifies at a lower temperature than Ni alloy. Moreover, both alloys solidify to chemically disordered crystalline structures, of which the Ni structure is less ordered than the Fe structure. Preliminary oxidation simulations of slab structures with single grain indicate that the dynamics of matrix/grain mixing processes have a pronounced influence on the oxidation reactions. We find that Al and Ni atoms in their unmixed state are the most active reactants towards oxygen, while the Al/Ni alloy and pure Fe layers show substantially slower oxidation kinetics. © 2013 AIP Publishing LLC. [<http://dx.doi.org/10.1063/1.4812387>]

I. INTRODUCTION

Current coal combustion technologies are known to have insufficient energy production efficiency and suffer from high CO_2 emissions. To tackle these issues, new technologies have been proposed. Many of these technologies, like advanced gasification systems, advanced oxy-fuel combustion systems, advanced ultra-supercritical steam systems, advanced turbine systems, and advanced carbon capture systems, require cost-effective structural and functional materials that can withstand the aggressive environments associated with the operating conditions of these systems.^{1,2} The performance of the materials in these harsh environments will strongly depend on the reactions that occur at surfaces. For example, the performance of structural components (such as a boiler tube or a turbine blade) will be affected by surface oxidation and corrosion processes. Excessive oxidation and corrosion may not only limit the life expectancy of the materials but may also compromise the mechanical integrity of the components due to underlying changes to their chemical structure. Therefore, understanding surface phenomena and engineering cost-effective materials that can withstand or control these processes are of paramount importance for the development of advanced engineering systems. Complex materials structures (e.g., multi-component or multi-phase materials) offer distinct

advantages over single component or single phase materials, as the properties of complex structures can be tailored or tuned by the appropriate combination and distribution of elements, constituents, or phases.

A general focus of research related to these issues is on the bulk and surface characteristics of $\text{Al}_x\text{Ni}_y\text{Fe}_{(1-x-y)}$ alloys, relevant to their use as structural materials in the presence of ambient gases (O_2 , H_2 , H_2O , and CO_2).^{3,4} A specific aim of these studies is to computationally predict the critical Al content necessary for Al_2O_3 scale formation and to predict oxidation growth kinetics. In this sense, it is important to study the stability of different sized Al grains in a Ni or Fe bulk matrix at temperatures above and below the structure melting point, which is the focus of this study.

Numerous theoretical studies in Ni-Al and Fe-Al compounds have been published. These include calculation of Ni-Al alloy properties, like phase stability,⁵ point defect properties,⁵ antiphase boundary energies,⁵ surface energies,⁵ relaxations,⁵ elastic constants for Ni_3Al ,⁵ as well as equilibrium lattice constants,⁶ cohesive energy,⁶ activation, and migration energies for self-diffusion and the vacancy jump processes for NiAl and Ni_3Al ,⁶ using the embedded atom method (EAM)⁷ in static (0 K),⁵ Monte Carlo (MC),^{5,8} or molecular dynamics (MD)^{6,8} calculations. The modified EAM potentials based on the second nearest-neighbor model (2NN MEAM)⁹ have also been used for Fe-Al binary alloys,

capable of reproducing ordering (DO_3 or $\text{B}2$),⁹ point defect formation,⁹ stacking fault energy,⁹ grain boundary segregation,⁹ and interactions between dislocations and solute atom,⁹ as well as structural, elastic, and thermodynamic properties.⁹ Other approaches have been employed as well, e.g., analysis of atomic ordering mechanism and order-disorder transformation phenomena (673–1273 K temperature range) in Fe_3Al type intermetallics by combining the electronic theory of alloys in pseudopotential approximation with MC simulation,¹⁰ or semi-empirical n-body non-central potential MD simulations of cluster formation and order transformations in the process of quick solidification of liquid $\text{Fe}_{50}\text{Al}_{50}$.¹¹ Regarding Al-Ni and Al-Fe diffusion processes specifically, there are multiple related studies published.^{12–26} Most of these studies deal with Al-Ni alloy diffusion at temperatures below the melting point. The diffusion of metal atoms at the Ni/Al planar interface has also been studied at temperature close to melting point using EAM potentials.²⁷ However, to the best of our knowledge, no previous studies have been examined the mixing process of Al grain in a Fe and Ni matrix.

In the present study, we investigate the grain matrix diffusion using MD with the ReaxFF empirical reactive force field for Fe, Ni, and Al.^{28,29} The motivation for using ReaxFF instead of EAM or other methods available is primarily related to the intended further simulations of Fe/Ni/Al alloy oxidation in the presence of ambient gases and the high quality of its previous performance in simulations on surface segregation in Fe/Ni/Al alloys.³⁰ We have recently demonstrated that ReaxFF can provide an accurate description for single-metal phases³¹ and compared the ReaxFF description for gold to EAM-descriptions for this metal,³² demonstrating that ReaxFF is of similar or superior quality (for diffusion barriers) to existing EAM descriptions. ReaxFF has a considerable higher computational expense than EAM or MEAM description (typically 5–20 times more expensive). Although the lower computational expense of the embedded atom descriptions may make these methods more appealing for single-metallic or simple bimetallic descriptions, for connection to gas-phase chemistry and carbide/hydride/oxide/sulfide chemistry,^{33–36} the high transferability and accuracy of the ReaxFF force field provide sufficient compensation for the increased computational expense.

II. METHOD

A. The ReaxFF reactive force field

The ReaxFF reactive force field²⁸ divides the potential energy of the system into various partial energy contributions, including bonding, over- and under-coordination, valence angle, penalty (for systems with two double bonds sharing an atom in a valence angle), torsion angle, conjugation (for systems with regions of overlapping p-orbitals), van der Waals, and Coulomb energies. The implementation of the energy terms is described below.

The bond order between a pair of atoms is obtained directly from the interatomic distance. The bond orders are corrected for over-coordination and for residual 1–3 bond

orders in valence angles, if applicable. The bonding energy is calculated as a function of bond orders.

After correction of the original bond orders, a degree of over-coordination may remain in the molecule. Therefore, the over-coordination energy imposes an energy penalty on the system as a function of the degree of deviation of the sum of the corrected bond orders around an atomic center from its valence. The form of the function ensures that over-coordination energy quickly vanishes to zero for under-coordinated systems.

For an under-coordinated atom, the energy contribution for the resonance of the π -electron between attached under-coordinated atomic centers is taken into account. This is done if the bonds between an under-coordinated atom and its under-coordinated neighbors partly have π -bond character.

Similarly to other bond-order dependent energy terms, the energy contribution from valence angle terms goes to zero as the bond orders in the valence angle go to zero. The effects of over/under-coordination in the central atom on the valence angle energy are taken into account. The equilibrium angle depends on the sum of π -bond orders around the central atom.

The torsion angle energy definition also accounts for the involved atom bond orders. A valence-angle-dependent term ensures that the torsion energy contribution disappears when either of the two valence angles approaches π .

To account for repulsive interactions at short interatomic distances due to Pauli exclusion principle and attraction energies at long distances due to dispersion, non-bonded interaction energies are defined. These interactions, corresponding to van der Waals and Coulomb forces, are included for all atom pairs, thus, avoiding abrupt alterations in the energy description during bond dissociation. For the van der Waals interactions, a distance-corrected Morse-potential is used. By including a shielded interaction, excessively high repulsions between bonded atoms (1-2 interactions) and atoms sharing a valence angle (1-3 interactions) are avoided. To adjust for orbital overlap between atoms at close distances, a shielded Coulomb potential is used to account for the Coulomb (electrostatic) interactions. Atomic charges are calculated using the Electron Equilibration Method (EEM) approach.⁶ According to it, the effective electronegativity of an atom in a molecule, which is equal to the molecular electronegativity, is expressed as a function of electronegativity and hardness of the neutral atom, as well as charges and interatomic distances between the atoms in the molecule. The electronegativity and hardness of an atom are defined as the first and second derivatives, respectively, of the total molecular energy with respect to the number of electrons associated with the atom.

Both molecular static and MD calculations can be carried out with ReaxFF. For the static calculations, the steepest descent and conjugate gradient minimization methods are available. For the dynamic calculations, the Verlet velocity algorithm⁸ is used to solve the Newtonian equations of motion. The MD calculations can be performed in NVE (constant system size-volume-energy) or microcanonical, NVT (constant system size-volume-temperature), a.k.a. canonical, and NPT (constant system size-pressure-temperature)

ensemble conditions. Velocity and system volume scaling (for NVT and NPT ensembles, respectively) is performed using the Berendsen method.³⁷ The main user choice for this method is the setting of the damping constants, which determine the strength of coupling between the system and an external velocity (heat) or volume (pressure) bath. High coupling (<100·t_{step} for NVT, <1000·t_{step} for NPT³⁸) may cause unphysical velocity distribution of the system.

B. Origin of Fe/Ni/Al parameters

The ReaxFF Fe/Ni/Al parameters were fitted against quantum mechanical (QM) calculations. These first-principles calculations were performed for ordered Fe/Al/Ni alloy phases using the plane-wave basis projector augmented wave (PAW) method and Perdew-Burke-Ernzerhof (PBE) for the exchange-correlation functional as implemented in the Vienna *Ab initio* Simulation Package (VASP). The QM data include equations of states of various compositions of Fe-Al, Ni-Al, and Fe-Ni crystal phases. The relationship between volume and energy of the bulk phase was investigated over a wide range of volume. The enthalpy of formation of ordered phases was also considered because the enthalpy of formation is important in evaluating the phase diagram through the thermodynamic modeling.

In addition to the parameterization of the ReaxFF force field with bulk properties of Fe/Al/Ni alloys, we also investigated binding energies and surface free energies on various metal surfaces to obtain the force field capable of describing the surface reactions as well as bulk properties. In order to evaluate the surface free energy, the semi-infinite bulk surface system was modeled by a slab consisting of 6 atomic layers parallel to the surface. To study the stabilities of different surface terminations, we compared the surface free energies of the surfaces with different stoichiometry. Further, we added adsorption energy of Al or Fe on interesting adsorption sites, e.g., bridging, hollow, face-centered cubic (fcc), and hcp sites on Fe or Al metal surfaces and re-trained the force field. A full description of this ReaxFF development process is given in Ref. 29.

C. MD-simulations

MD type simulations in combination with the ReaxFF empirical reactive force field, using the ADF/ReaxFF implementation, have been performed in the study. Prior to the MD simulation, we prepared conjugate gradient energy minimized (force tolerance/root mean square of potential energy less than 0.25 kcal/mol/Å) periodic bulk structures of pure Fe(bcc) and Ni(fcc) with sizes of 2000 and 2048 atoms, respectively. Subsequently, 1 and 8 spherical Al grains were defined in the Fe and Ni matrices, yielding approximate grain/matrix atom ratio of 1:3, by substituting the respective bulk subvolume atoms with Al atoms (Table I and Figure 9 in the Appendix). Since the interatomic distances in pure Al crystals are longer than those of Fe and Ni (Table II), it was required to relax the newly defined grain/matrix structures through an energy minimization process (no volume change allowed during the minimization). Note that we are using

TABLE I. Atomic percentage of Al in Fe/Ni-Al matrix/grain structures.

Matrix	at. % Al	
	1 grain	8 grains
Fe	25.1	28.0
Ni	23.6	26.6

simple spherical grain-shapes here (Sec. III F)—in future studies, we aim to expand these simulations and employ larger, Wulff reconstructed subsurface clusters.^{39–41}

The isothermal–isobaric ensemble (NPT), in implementation with the Verlet velocity algorithm for integrating the equations of motion⁸ and the Berendsen thermo/barostat,³⁷ has been used in this study. Settings of 0.25 fs time step, 100 fs temperature, and 5000 fs pressure damping constants were used. The atmospheric pressure was set to 0 Pa during the whole simulation. To simulate heating process of the structures in the temperature range of 300 to 3000 K, the temperature was changed stepwise by 100 K increments after 50 ps equilibration time intervals. Cooling simulations were also performed with the structures obtained from 1 Al grain melting simulations over the temperature range of 3000–300 K using the same simulation settings.

The oxidation simulations of the Ni and Fe slab structures with a single Al grain were modeled by randomly introducing 3000 oxygen molecules into the slab vacuum with the initial oxygen density of 0.09 kg/l in constant volume and temperature (NVT) ensemble at 1500 K. Settings of 0.1 fs time step and 300 fs temperature damping constant with individually damped atoms were used. The temperature damping was applied to the slab atoms only.

1. Strain energy definition

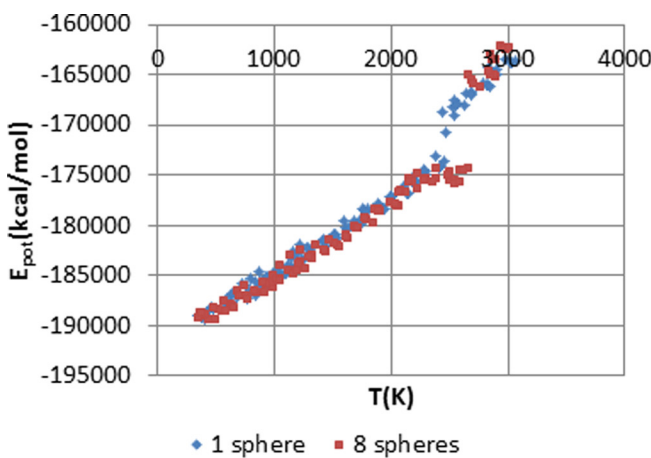
The chemical strain energy per atom is defined as the sum of the total potential energy component fractions per atom subtracted by the heat of formation increment, which corresponds to the energy of the respective atom type in its natural state. The potential energy component fractions are defined specifically for each energy component.

III. RESULTS AND DISCUSSION

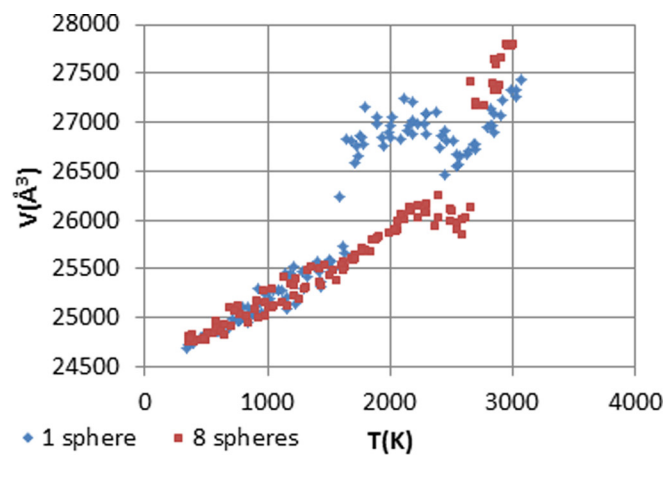
For analysis of results, the potential energies and system volumes vs. temperature were plotted (Figures 1–6). These enabled us to detect time instants when critical changes in the structures occur. Also, locally calculated chemical strain energies per atom (Figures 10–13 in the Appendix) as well

TABLE II. Characteristic temperatures and bond distances of Ni, Fe, and Al.

	m.p. (K) ^{48,49}	b.p. (K) ^{48,49}	bond dist. (Å)
Ni	1726	3157	2.489
Fe	1811	3134	2.459
Al	933	2792	2.863 (Ref. 50)



(a)



(b)

FIG. 1. Potential energy (a) and volume (b) vs. temperature for Fe matrix structures during heating.

as the radial distribution function (RDF) and its integral form (IRDF) were evaluated (Figures 18–21, 26 and 27 in the Appendix). For visualization of strain energy and atom distribution, graphical snapshots of the structure cross sections at different time instants were used.

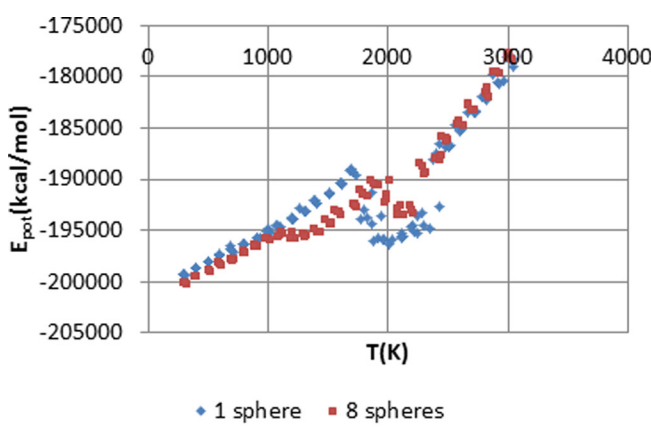
A. Potential energy, volume, and atom distribution during melting

For the 1 Al grain-Fe matrix structure, the volume rise at about 1600 K (Figure 1(b) and Figures 10(a) and 10(b) in the Appendix) could correspond to melting of Al (Figure 18(a) in the Appendix), due to substantial Al-Al RDF peak flattening, and interface mixing (Figures 18(c) and 18(d) in the Appendix), due to increase in Fe-Al RDF and IRDF values. The potential energy rise and volume drop at about 2500 K (Figure 1 and Figures 10(c) and 10(d) in the Appendix) could correspond to complete grain/matrix atom mixing (Figures 18(c) and 18(d) in the Appendix), due to substantial increase in Fe-Al RDF and IRDF values, and structure melting (Figures 18(a) and 18(b) in the Appendix), due to notable Al-Al and Fe-Fe RDF peak flattening. Similar

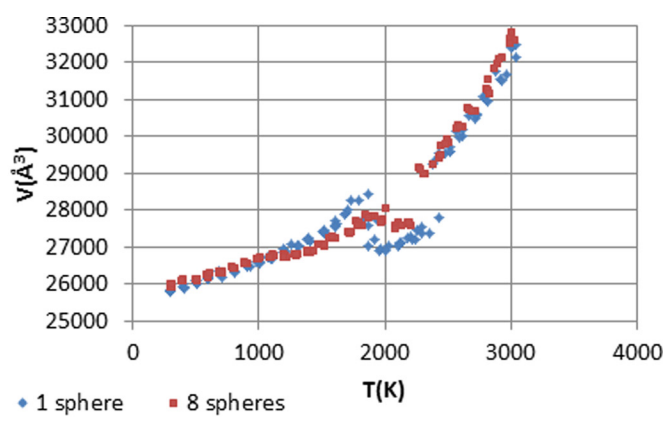
reasoning applies to the conclusions that follow for the other Fe and Ni matrix structures.

For the 8 Al grain-Fe matrix structure, we observed the slight potential energy and volume drop after reaching 2300 K (Figure 1 and Figures 11(a) and 11(b) in the Appendix) during the substantial interface mixing (Figures 19(c) and 19(d) in the Appendix) and melting of Al (Figure 19(a) in Appendix). A sharp rise of potential energy and volume at about 2700 K (Figure 1 and Figures 11(b) and 11(c) in the Appendix) is due to complete grain/matrix atom mixing (Figures 19(c) and 19(d) in the Appendix) and structure melting (Figures 19(a) and 19(b) in the Appendix).

For the 1 Al grain-Ni matrix structure, the potential energy and volume drop at about 1800 K (Figure 2 and Figures 12(a) and 12(b) in the Appendix) could result from partially ordered mixing of grain/matrix atoms in the grain region (Figures 20(c) and 20(d) in the Appendix), which was not observed for Fe matrix structures, and structure melting (Figures 20(a) and 20(b) in the Appendix), particularly Al grain. The partially ordered mixing is attributed to a large increase in the first peak and small change between the first and second peaks of the Ni-Al



(a)



(b)

FIG. 2. Potential energy (a) and volume (b) vs. temperature for Ni matrix structures during heating.

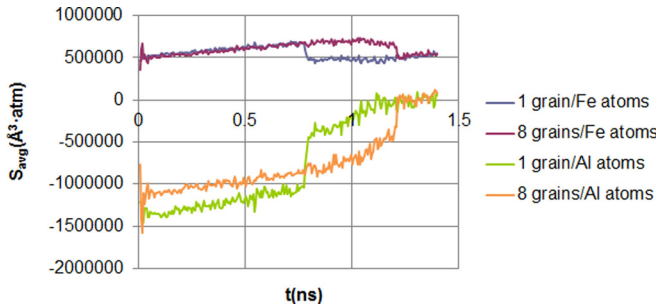


FIG. 3. Mean atomic hydrostatic stress [$\text{\AA}^3\cdot\text{atm}$] vs. time for 1/8 Al grain Fe matrix structures during heating.

RDF, and the corresponding increase and flatness of the first coordination shell segment of the Ni-Al IRDF. The potential energy and volume rise at about 2400 K (Figure 2 and Figures 12(b) and 12(c) in the Appendix) could result from complete mixing of grain/matrix atoms (Figures 20(c) and 20(d) in the Appendix) and dynamic continuation of structure melting (Figures 20(a) and 20(b) in the Appendix).

For the 8 grain-Ni matrix structure, the discontinuation of the increase of volume and potential energy at about 1000 K (Figure 2 and Figures 13(a) and 13(b) in the Appendix) could be related to the initiation of grain/matrix atom mixing (Figures 21(c) and 21(d) in the Appendix) and structure melting (Figures 21(a) and 21(b) in the Appendix). Further drop in volume and potential energy at about 2000 K (Figure 2 and Figures 13(c) and 13(d) in the Appendix) could be related to more dynamic mixing (Figures 21(c) and 21(d) in the Appendix) and melting (Figures 21(a) and 21(b) in the Appendix) processes. Subsequent sharp rise in volume and potential energy at about 2300 K (Figure 2 and Figures 13(d) and 13(e) in the Appendix) could be related to complete mixing of grain/matrix atoms (Figures 21(c) and 21(d) in the Appendix) and structure melting continuation (Figures 21(a) and 21(b) in the Appendix).

Summarizing the above observations, it could be concluded that

- The Al grains start melting earlier than matrix atoms in accordance with the lower melting point of Al (Table II).

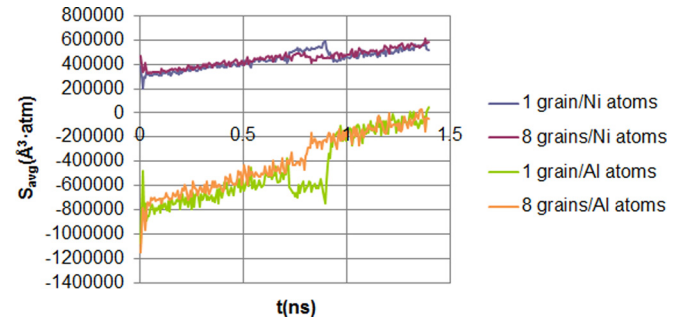


FIG. 4. Mean atomic hydrostatic stress [$\text{\AA}^3\cdot\text{atm}$] vs. time for 1/8 Al grain Ni matrix structures during heating.

- Sudden changes of volume and potential energy accompany initiation of abrupt changes in structure melting and mixing processes, which most often coincide.
- In the Fe matrices, grain/matrix melting and mixing occur earlier for larger grains, supposedly due to the latter having a sharp expansion prior to the matrix melting start, which is not observed in any of our other simulations and could be related to Fe-Fe crystal bond lengths being shorter than Ni-Ni bond lengths, both being smaller than those of Al-Al (Table II), thus, creating a larger volume mismatch in the Fe/Al case, compared to the Ni/Al case. Likewise, the sharp expansion could be related to Al atoms, which are most stable in FCC configuration, in Fe matrix initially being in a body-centered cubic (BCC) configuration instead of FCC configuration in the Ni matrix case. Both effects are related to the applied grain definition (Sec. II C).
- In the Ni matrices, melting and mixing occur earlier for smaller grains, supposedly due to the latter having a larger interface area.
- Mixing is generally complete for Ni matrix at lower temperature than for Fe matrix in accordance with the lower melting point of Ni.
- Differences in mixing temperature, energy/volume change patterns, and partially mixing favorable grain sizes for Fe and Ni matrices could be attributed to differences in

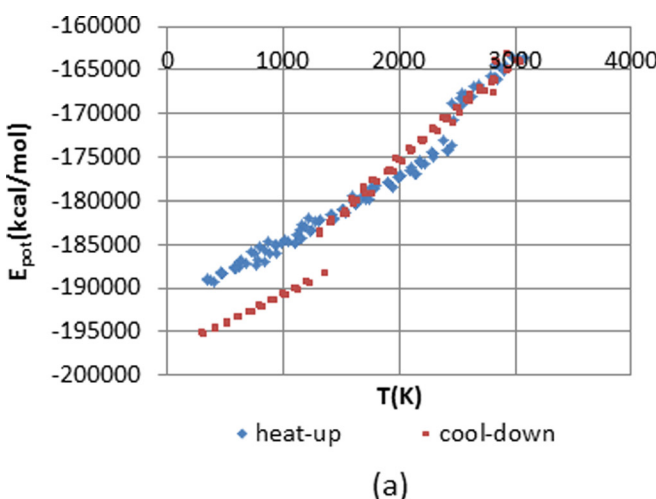


FIG. 5. Potential energy (a) and volume (b) vs. temperature for 1 Al grain Fe matrix structure during heating and cooling.

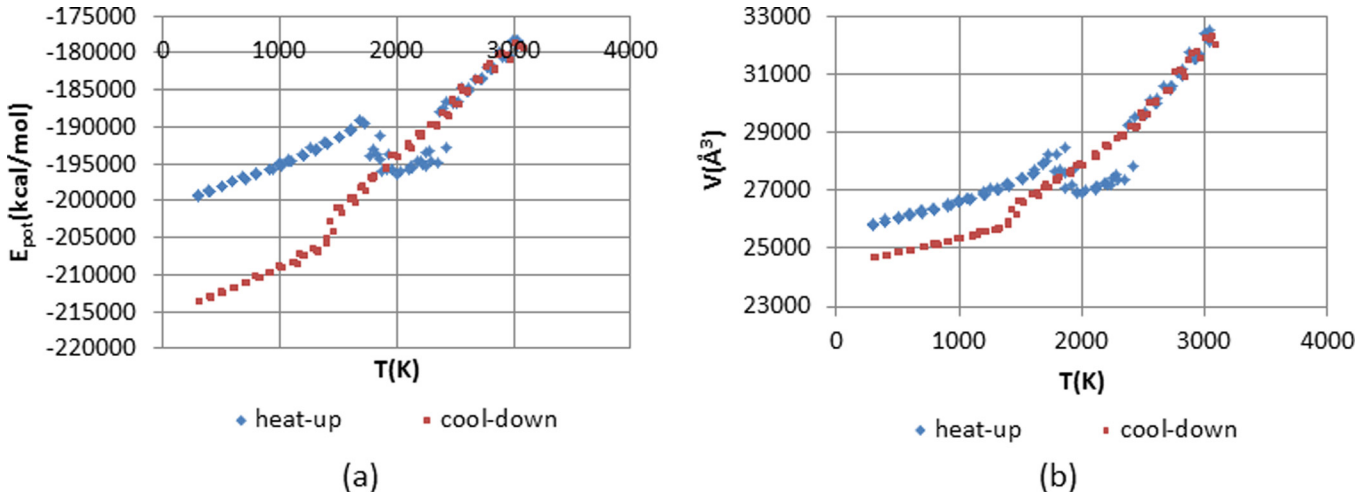


FIG. 6. Potential energy (a) and volume (b) vs. temperature for 1 Al grain Ni matrix structure during heating and cooling.

mixing/formation energies, which are about -19 kJ/mol (Ref. 42) for Fe_3Al and about -41 kJ/mol (Ref. 43) for Ni_3Al at 0 K . The observations are in accord with the strain energy distribution, described below.

- Structure melting processes occur primarily at higher temperatures than the known melting points of the metal components (Table II), which could be partially attributed to the heating rate.

From the system snapshots (Figures 10–13 in the Appendix), it can be concluded that initial volume diffusion primarily occurs when the matrix atoms migrate into the molten Al grain with comparatively less Al atoms migrating into the matrix, which conforms with the results published in Ref. 27.

B. Strain energy distribution during melting

The relative stability of atoms can be estimated based on their chemical strain energy values, as defined in Sec. II C. The atoms with lower strain energy are considered to be more stable. However, the strain energy definition does not allow for absolute value comparison between different atom types.

From the chemical strain energy distribution for matrix atoms (Figures 10–13 in the Appendix), ranging approximately between 0 and $40\text{--}60 \text{ kcal/mol}$ for both matrices, it can be observed that the matrix atoms at the grain/matrix interface are less stable than the bulk atoms. The chemical

strain energy of Al atoms ranges approximately between -70 and 0 kcal/mol for Ni matrix and between -30 and 10 kcal/mol for Fe matrix. This allows for the conclusion that Al atoms are comparatively more stable in Ni matrix, which likewise could be attributed to the differences in mixing/formation energies. In distinction to matrix atoms (Figures 10–13 in the Appendix), the Al atoms appear to be more stable, compared to bulk, at grain/matrix interface. For all atom types, the stability differences increase as the temperature increases.

C. Stress distribution during melting

Supplemental hydrostatic stress distribution calculations were performed during the melting simulations. For that purpose, the individual atom stress components were calculated using the LAMMPS/ReaxFF implementation, which calculates the per-atom stress, defined as the negative of the per-atom pressure tensor, in units of stress \times volume. The compatibility of the LAMMPS and the ADF/ReaxFF implementations was verified by comparing the respective potential energy and volume vs. time plots. Stresses were calculated from the potential energy force contributions with the kinetic energy contributions excluded.⁴⁴ The stress distribution plots (Figures 14–17 in the Appendix) indicate that distinct compressive or tensile stress regions are present only prior to the initiation of mixing and melting processes. Furthermore, the Al atoms appear to be in compression,

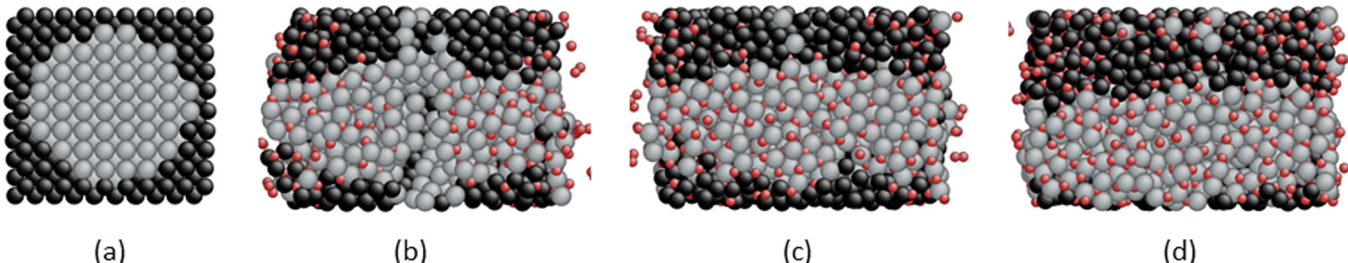


FIG. 7. Fe matrix/1 Al grain structure oxidation simulation snapshots (Fe—black, Al—grey, O—red).

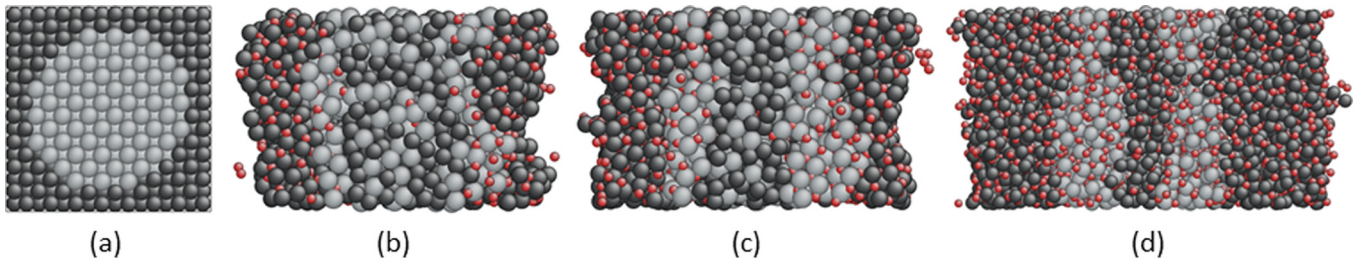


FIG. 8. Ni matrix/1 Al grain structure oxidation simulation snapshots (Ni—black, Al—grey, O—red).

whereas the matrix atoms are in tension, which is attributed to the differences in bond lengths, as discussed in Sec. III A, and partially related to the strain energy differences. Due to the increasingly randomized stress distribution after melting initiation, the mean and standard deviation values for each atom type were calculated from the atomic stresses at each iteration. By comparing the potential energy and mean stress changes vs. temperature and time, respectively, temperature and time axes being considered equivalent due to the linear heating rate (Figures 1–4), it was concluded that the mean stress changes abruptly upon discontinuous volume change, but not upon discontinuous potential energy changes in melting/mixing processes which do not involve sharp volume change. During the rest of mixing and melting processes, the mean stresses for matrix atoms increase gradually, implying higher tension due to heating, whereas for the Al atoms, the mean stress values approach zero, which could be considered as approaching tensile deformation state, compared to the initial state of compression.

Likewise, it can be observed that initially the Al/matrix atom stress ratio is greater than 1, but after melting and mixing it becomes much smaller than 1. That can be related to the NPT ensemble setting of zero total pressure (hydrostatic stress), which does include the kinetic energy contribution; the Al/matrix stoichiometric ratio of 1:3, which requires that the mean Al/matrix hydrostatic stress ratio should be 3:1; differences in strain energy stability, which intensify at higher temperatures, and comparatively small kinetic energy contribution at low temperatures. In distinction to the mean stress values, the stress dispersion/scattering, characterized by the standard deviation of stress for all atoms, increases at constant rate (Figures 22 and 23 in the Appendix), except for discontinuous changes at moments of abrupt volume or potential energy change (Sec. III A), until an asymptotic value is approached. This could be attributed to the increase in kinetic energy in combination with the phase change. The large final standard deviation values suggest that, upon solidification, residual stresses larger than the initial stresses might occur, with matrix atoms being primarily in tension.

D. Solidification analysis

The molten Al/Ni and Al/Fe alloy simulations (Figures 5 and 6) indicated that transitions from liquid to solid state, characterized by discontinuous drop in potential energy and volume, occurred for the Fe alloy at about 1200 K and 1400 K for Ni, which is between the melting points of Al and Fe/Ni, respectively. The difference of order of 1000 K

between the melting and solidification temperatures of both alloys could be explained by both superheating and undercooling effects due to the applied high heating and cooling rates, respectively (stepwise temperature increments/decrements of 100 K with 50 ps equilibration time intervals, corresponding to uniform heating/cooling rate of 2×10^{12} K/s). Furthermore, the Fe alloy indicates a single-crystalline structure (Figures 26 and 24 in the Appendix), due to close to zero values between the first and second peaks of all (Fe-Fe, Al-Al, Fe-Al) RDFs and the corresponding flat segment for the first coordination sphere in the Fe-Al IRDF, whereas the Ni alloy has a polycrystalline/fine-grained structure (Figures 27 and 25 in the Appendix), due to less distinct crystalline structure patterns in all (Ni-Ni, Al-Al, Ni-Al) RDFs, particularly Al-Al, and the Ni-Al IRDF. It is known that for Ni-Al alloys the degree of order, composition of the solidified structure, and transition to amorphous vs. crystalline state are dependent on cooling rate as well as the liquid alloy composition. For the Ni alloy, in particular, the cooling rate (2×10^{12} K/s), that was used in the simulation, corresponds to the critical range of rates for crystalline structures,⁴⁵ whereas the specific solidification temperature corresponds to the dominance of chemically disordered FCC phase.⁴⁶ However, the existence of the chemically disordered Al/Fe alloy at temperature below 1173 K and 813 K is in conflict with the experimentally observed transition to the chemically ordered phases of B2 and DO₃,⁴⁷ respectively, which could be attributed to the effect of high cooling rate. Yet both structures yield energetically more stable, i.e., having a lower potential energy, final configurations compared to the initial ideal-crystalline structures (Figures 5(a) and 6(a)), which conforms with the negative formation energy for both Ni-Al and Fe-Al alloys,^{42,43} the approximate ratio of total heating/cooling potential energy change $dE_{\text{pot}}(\text{Ni-Al})/dE_{\text{pot}}(\text{Fe-Al})$ —2.4—being close to the ratio of formation energies of the respective alloys—2.2.

E. Preliminary oxidation simulation results

We performed a series of MD-simulations on the Fe/Ni matrix/1 Al grain systems, defined in Sec. II C, in order to study the influence of grain/matrix mixing on oxidation kinetics.

The Fe matrix simulations (Figure 7) indicate that oxygen preferably reacts with Al, which melts before active mixing occurs. This accounts for the observed oxygen diffusion inwards the slab. At the same time, the Fe matrix atoms remain primarily in a crystalline state and are oxidized comparatively slowly. The final oxidation states for Fe and

Al are 1.7 and 3.3, respectively, which suggests that oxidation is complete for Al, whereas Fe is underoxidized, according to assumed stoichiometry of Al_2O_3 and FeO , the latter corresponding to the lowest Fe oxidation state.

The Ni matrix simulations (Figure 8) reveal that initially oxygen reacts with unmixed Ni and Al atoms in the outer surface layers, whereas inside the slab rapid matrix/grain mixing occurs without notable oxygen diffusion taking place. This suggests that Ni-Al alloy might be less reactive with oxygen than pure Ni or Al structures. It can also be observed that mixing is not complete, resulting in formation of rapidly oxidizing Al subsurface layers. In the final snapshot, it can be observed that Al from the alloy layer eventually has dissolved into the adjacent Al layers and subsequently a layer of Ni oxide in the middle of the slab has formed. Again, the oxidation is complete for Al (oxidation state of 3.1), whereas Ni is underoxidized (oxidation state of 1.7), according to assumed stoichiometry of Al_2O_3 and NiO . This allows for the conclusion that in the considered structures the oxidation rates of Fe and Ni are lower, compared to Al, the rate of Fe being the lowest.

The results of these small-scale, preliminary oxidation simulations indicate that the dynamics of matrix/grain mixing processes has a pronounced influence on the kinetics of oxidation reactions; we aim to report larger-scale MD-studies on this topic in the future.

F. System size considerations

Although the simulated systems can be regarded as small scale,^{51,52} it is believed that the observed differences in mixing favorable behavior (Secs. III A–III D) of Al nanograins in Fe or Ni matrices should hold also at higher length scale. This is supported by the similar results obtained for the two considered model grain sizes. However, it is also believed that larger scale studies are essential for realistic mesoscale estimate of mixing characteristics for alloys of identical composition, for which purpose the current study is considered as small scale validation prerequisite.

IV. SUMMARY

To study the stability of different sized Al grains in Ni/Fe bulk matrices at temperatures above and below the structure melting point, MD simulations of respective structures (grain/matrix atom ratio $\sim 1:3$) have been carried out in NPT ensemble conditions for temperatures being stepwise ramped over the range of 300–3000 K. The results show that, in accord with the published data, Al-Ni alloy is energetically more stable than Al-Fe alloy. This is confirmed by lower chemical strain energy for Al in the Ni alloy and completion of Al-Ni mixing at a lower temperature for the Fe matrix. Supposedly due to Fe-Fe crystal bond lengths being shorter than Al-Al bond lengths, larger Al grains appear to be favorable for mixing with Fe matrix. However, for Ni matrix, smaller Al grains appear to be favorable for mixing, which can be explained by larger interface/mixing area, differences in the heat of formation and Ni-Ni crystal bond lengths being longer than Fe-Fe bond lengths.

Supplemental hydrostatic stress distribution calculations during the melting simulations were performed to check for

any correlation between stresses and the chemical strain energy distribution, as well as changes of stress distribution at moments of dynamic melting and mixing. The calculations indicate that a relation between strain energy stability and stresses for matrix and grain atoms exists both before and after structure melting. The stress value scattering, characterized by the standard deviation of stresses, was found to be increasing with temperature. The obtained stress distribution could serve as an estimate of the residual stress levels, which would be obtained upon amorphous/polycrystalline solidification.

We also performed cooling simulations over the temperature range of 3000–300 K. These revealed that for the considered cooling rate Fe alloy solidifies at a lower temperature than Ni alloy. Moreover, the Fe alloy solidifies to a crystalline structure, whereas the Ni alloy solidifies to a polycrystalline/fine-grained structure. The approximate ratio of total heating/cooling potential energy change is found to be close to the ratio of formation energies of the respective Fe and Ni alloys.

The results of preliminary oxidation simulations of slab structures with a single Al grain allow us to conclude that the dynamics of matrix/grain mixing processes have a pronounced influence on the oxidation reactions. We find that Al and Ni atoms in their unmixed state are the most active reactants towards oxygen, while the Al/Ni alloy shows substantially slower oxidation kinetics. In contrast, Fe layers oxidize at a slower rate partially due to the formation of Al-O interfaces on the slab surfaces, which do not occur in the Ni matrix case.

ACKNOWLEDGMENTS

This research was sponsored by the National Energy Technology Laboratory, U.S. Department of Energy, under Award No. DE-FE0005867. Furthermore, as part of the National Energy Technology Laboratory's Regional University Alliance (NETL-RUA), a collaborative initiative of the NETL, this technical effort was performed under the RES Contract No. DEFE0004000.

We wish to thank the PSU Research Computing and Cyberinfrastructure group for providing the computational resources.

This project was funded by the Department of Energy, National Energy Technology Laboratory, an agency of the United States Government, through a support contract with URS Energy & Construction, Inc. Neither the United States Government nor any agency thereof, nor any of their employees, nor URS Energy & Construction, Inc., nor any of their employees, makes any warranty, expressed or implied, or assumes any legal liability or responsibility for the accuracy, completeness, or usefulness of any information, apparatus, product, or process disclosed, or represents that its use would not infringe privately owned rights. Reference herein to any specific commercial product, process, or service by trade name, trademark, manufacturer, or otherwise does not necessarily constitute or imply its endorsement, recommendation, or favoring by the United States Government or any agency thereof. The views and opinions of the authors expressed herein do not necessarily state or reflect those of the United States Government or any agency thereof.

APPENDIX: CONFIGURATION SNAPSHOTS, ADDITIONAL ANALYSIS PLOTS

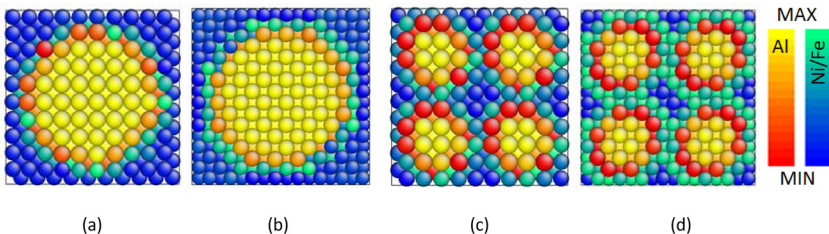


Figure	Fe		Al	
	min	max	min	max
a	-0.2812	3.9289	-23.0818	-4.4694
c	-0.3282	3.0271	-18.6820	-4.7794
Figure	Ni		Al	
	min	max	min	max
b	0.1385	4.3081	-45.0379	-2.4486
d	0.7103	4.2367	-22.1244	-5.3649

FIG. 9. Strain energy [kcal/mol] distribution for Fe (1 grain (a), 8 grains (c)) and Ni (1 grain (b), 8 grains (d)) matrix structures in the initial configuration at 300 K.

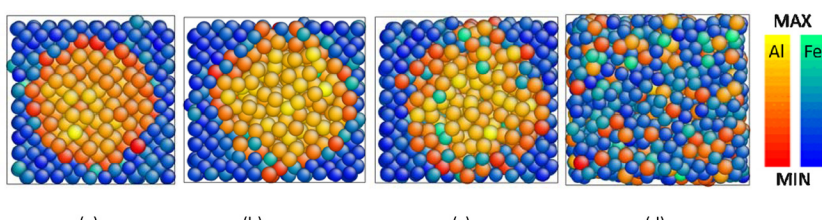


Figure	T(K)	Fe		Al	
		min	max	min	max
a	1437	-2.8121	22.3458	-23.0585	9.886
b	1781	-3.1055	33.7568	-27.6153	11.9302
c	2190	-2.0714	39.3965	-28.2012	12.2961
d	2560	-0.3379	42.5658	-35.411	6.8713

FIG. 10. Strain energy [kcal/mol] distribution for 1 Al grain in Fe matrix structure at different temperatures during heating.

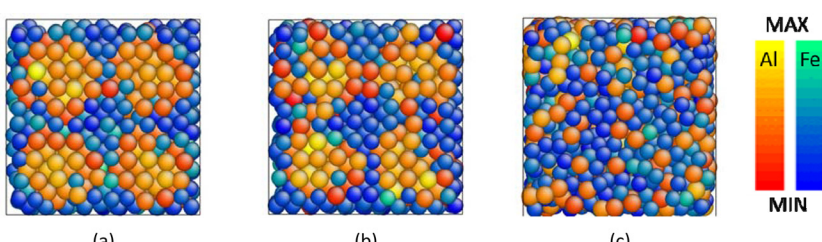
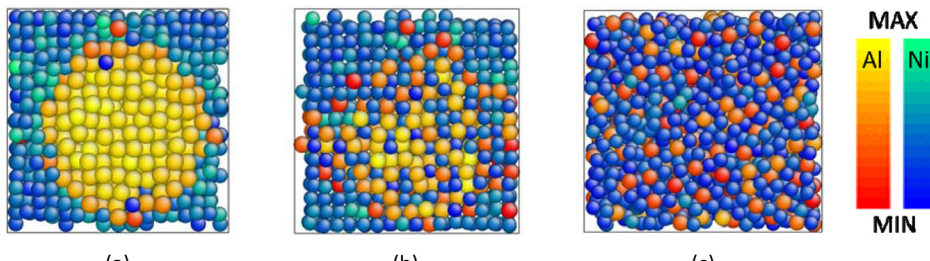


Figure	T(K)	Fe		Al	
		min	max	min	max
a	2218	-3.1305	35.0254	-30.6674	11.6543
b	2359	-1.3442	38.7948	-28.9295	5.9496
c	2827	2.6176	49.2919	-35.2037	12.9927

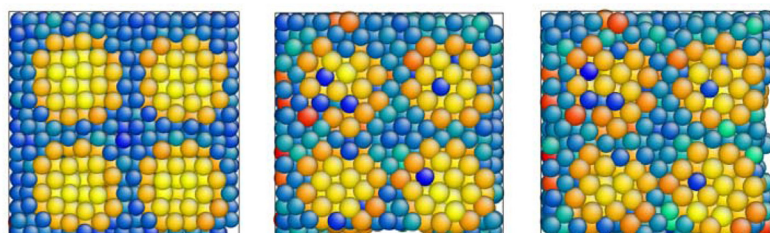
FIG. 11. Strain energy [kcal/mol] distribution for 8 Al grains in Fe matrix structure at different temperatures during heating.



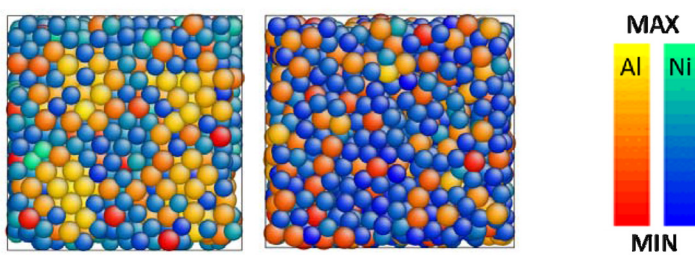
(a) (b) (c)

Figure	T(K)	Ni		Al	
		min	max	min	max
a	1599	-4.0874	18.458	-65.1115	4.2927
b	2006	-6.3304	24.9469	-68.2345	-5.4786
c	2371	2.3634	49.3437	-70.757	-9.2574

FIG. 12. Strain energy [kcal/mol] distribution for 1 Al grain in Ni matrix structure at different temperatures during heating.



(a) (b) (c) (d) (e)



(a) (b) (c) (d) (e)

Figure	T(K)	Ni		Al	
		min	max	min	max
a	977	-5.2219	21.0283	-72.3846	-2.5232
b	1378	-9.715	21.4779	-73.1757	1.9223
c	1783	-9.2235	23.0217	-69.7747	5.4961
d	2076	-8.9252	26.46	-72.0443	4.6963
e	2436	3.4853	41.9935	-71.6098	-6.648

FIG. 13. Strain energy [kcal/mol] distribution for 8 Al grains in Ni matrix structure at different temperatures during heating.

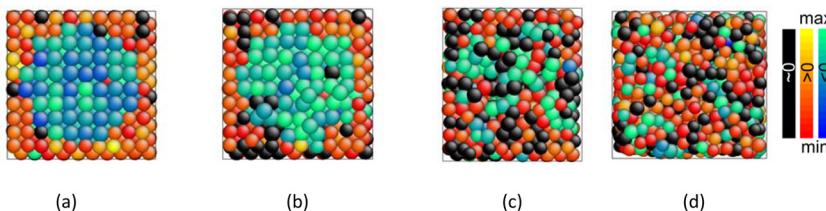


Figure	T(K)	t(ns)	Fe		Al	
			min	max	min	max
a	511	0.12	-1.00	1.98	-3.13	0.34
b	1575	0.68	-2.15	3.82	-4.48	2.20
c	2095	0.93	-2.69	4.29	-4.41	3.23
d	2671	1.24	-4.41	4.90	-5.07	3.97

FIG. 14. Atomic hydrostatic stress [$10^6 \text{ \AA}^3 \cdot \text{atm}$] distribution for 1 Al grain in Fe matrix structure at different temperatures during heating.

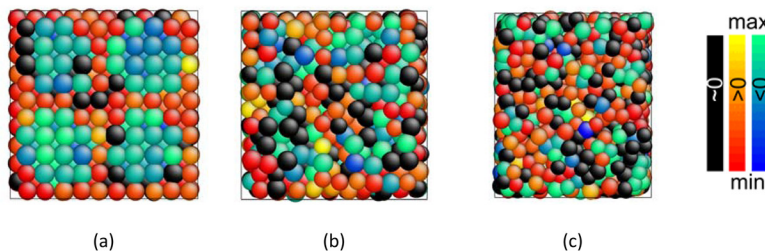


Figure	T(K)	t(ns)	Fe		Al	
			min	max	min	max
a	493	0.12	-1.06	2.63	-2.89	0.49
b	2438	1.06	-2.71	4.58	-3.99	3.26
c	2904	1.31	-5.95	5.37	-5.91	4.16

FIG. 15. Atomic hydrostatic stress [$10^6 \text{ \AA}^3 \cdot \text{atm}$] distribution for 8 Al grains in Fe matrix structure at different temperatures during heating.

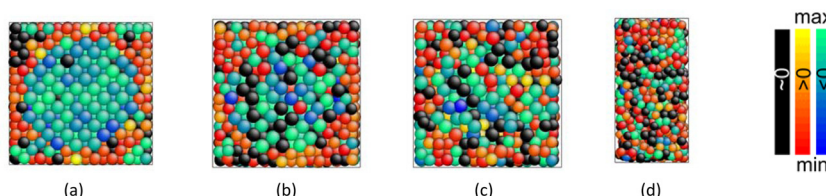


Figure	T(K)	t(ns)	Ni		Al	
			min	max	min	max
a	398	0.1	-1.24	1.88	-2.25	0.62
b	1403	0.6	-2.89	3.31	-2.97	1.27
c	1802	0.8	-3.35	3.58	-4.04	2.36
d	3071	1.4	-5.22	4.75	-6.08	3.17

FIG. 16. Atomic hydrostatic stress [$10^6 \text{ \AA}^3 \cdot \text{atm}$] distribution for 1 Al grain in Ni matrix structure at different temperatures during heating.

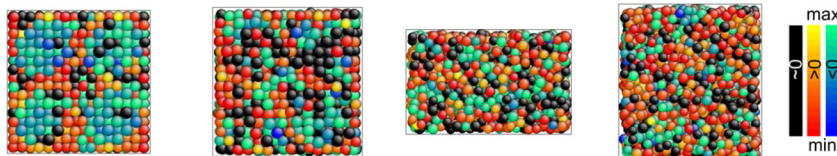


Figure	T(K)	t(ns)	Ni		Al	
			min	max	min	max
a	398	0.1	-1.34	1.86	-2.03	0.64
b	1590	0.7	-3.09	3.16	-4.13	1.78
c	1980	0.9	-6.65	3.86	-4.87	3.26
d	3000	1.4	-5.60	4.36	-4.86	3.31

FIG. 17. Atomic hydrostatic stress [$10^6 \text{ \AA}^3 \cdot \text{atm}$] distribution for 8 Al grains in Ni matrix structure at different temperatures during heating.

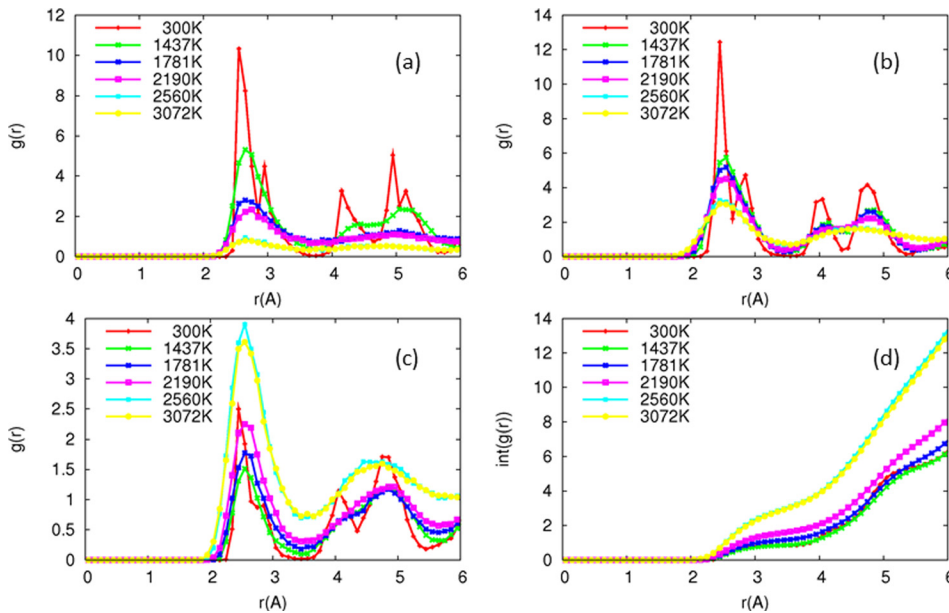


FIG. 18. RDF of Al-Al (a), Fe-Fe (b), Fe-Al (c), and IRDF of Fe-Al (d) for 1 Al grain in Fe matrix structure during heating.

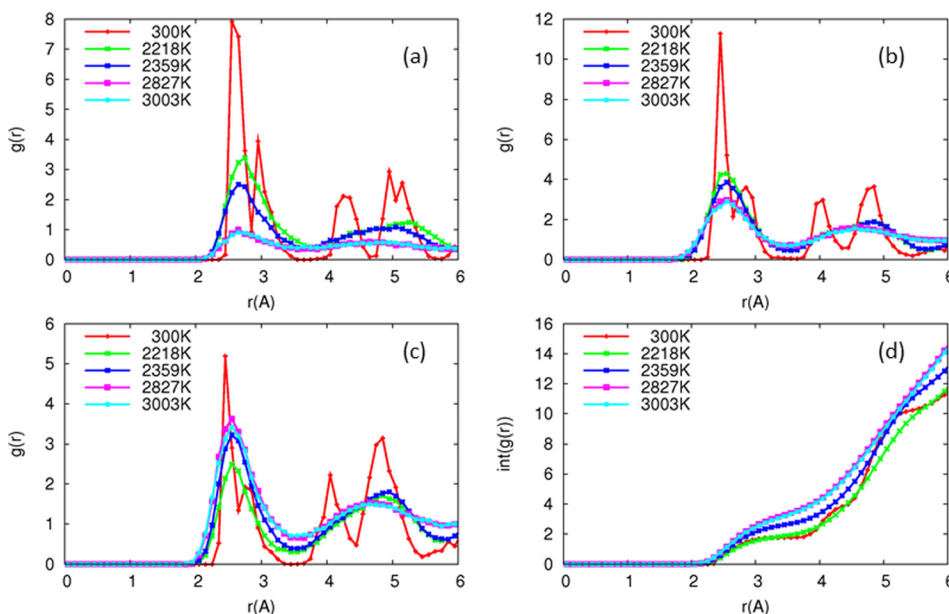


FIG. 19. RDF of Al-Al (a), Fe-Fe (b), Fe-Al (c), and IRDF of Fe-Al (d) for 8 Al grains in Fe matrix structure during heating.

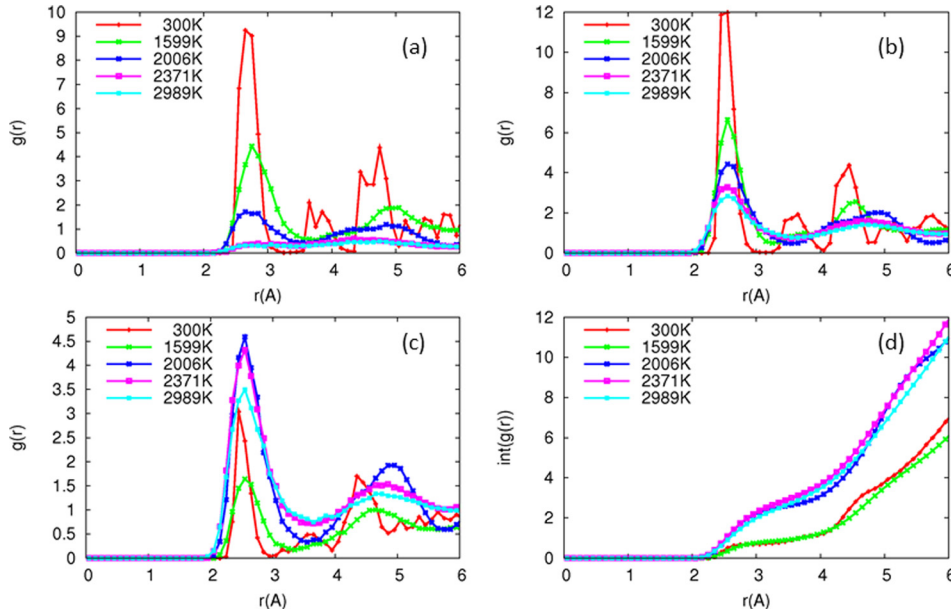


FIG. 20. RDF of Al-Al (a), Ni-Ni (b), Ni-Al (c), and IRDF of Ni-Al (d) for 1 Al grain in Ni matrix structure during heating.

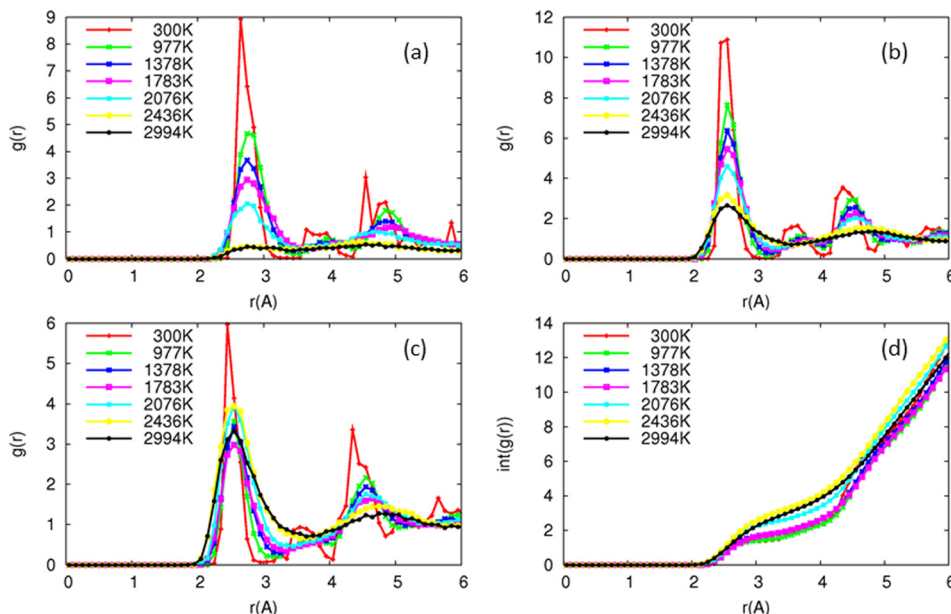


FIG. 21. RDF of Al-Al (a), Ni-Ni (b), Ni-Al (c), and IRDF of Ni-Al (d) for 8 Al grains in Ni matrix structure during heating.

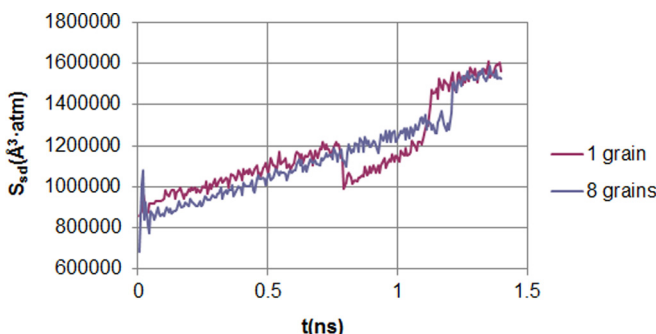


FIG. 22. Standard deviation of atomic hydrostatic stress [$\text{Å}^3 \cdot \text{atm}$] vs. time for 1/8 Al grain Fe matrix structures during heating.

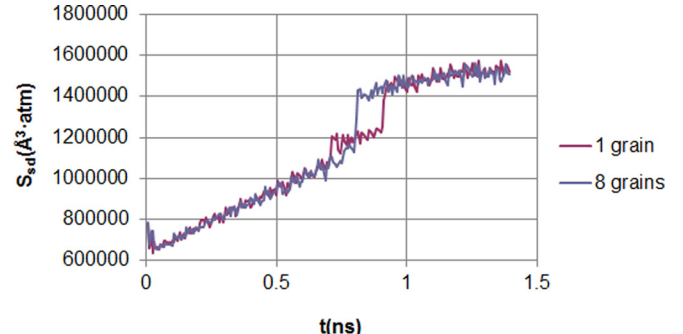
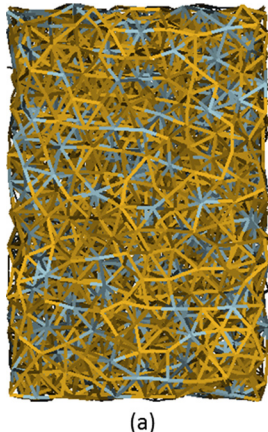
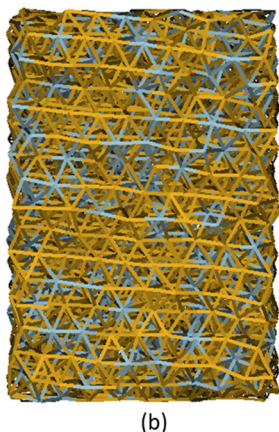


FIG. 23. Standard deviation of atomic hydrostatic stress [$\text{Å}^3 \cdot \text{atm}$] vs. time for 1/8 Al grain Ni matrix structures during heating.

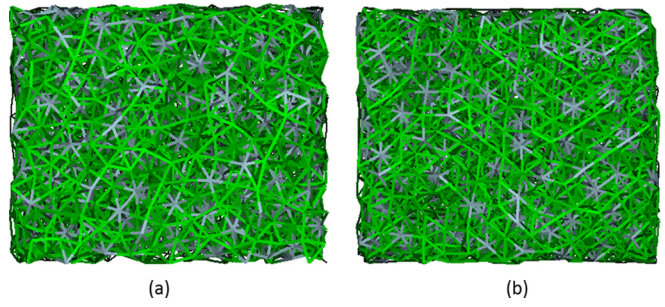
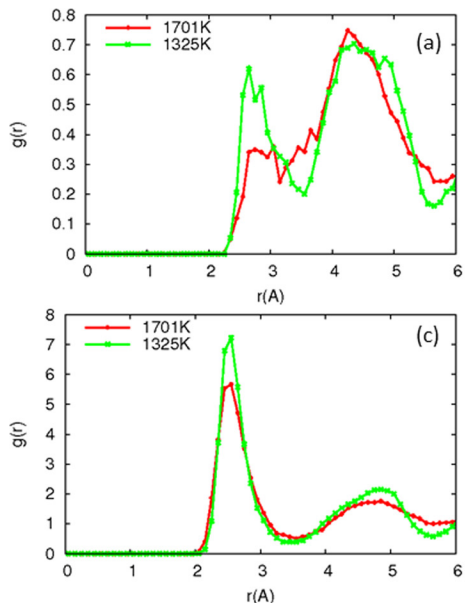
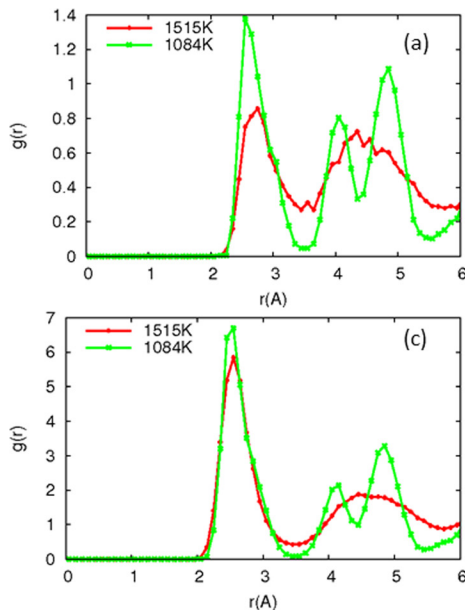


(a)



(b)

FIG. 24. Molten Fe matrix structure configuration snapshots before (1701K (a)) and after (1325 K (b)) solidification (Fe—orange, Al—grey).



(a)

(b)

FIG. 25. Molten Ni matrix structure configuration snapshots before (1515K (a)) and after (1084 K (b)) solidification (Ni—green, Al—grey).

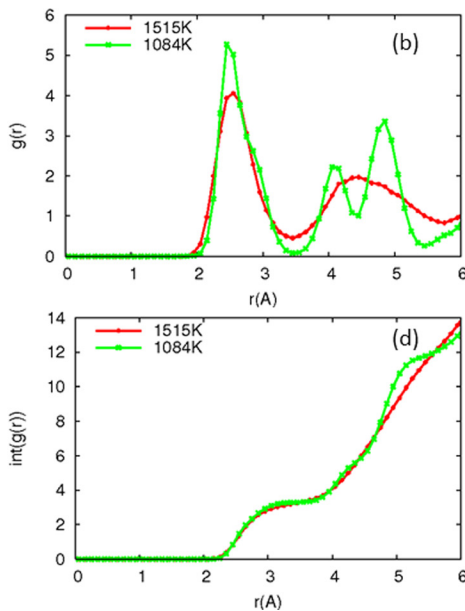


FIG. 26. RDF of Al-Al (a), Fe-Fe (b), Fe-Al (c), and IRDF of Fe-Al (d) for molten 1 Al grain in Fe matrix structure during cooling.

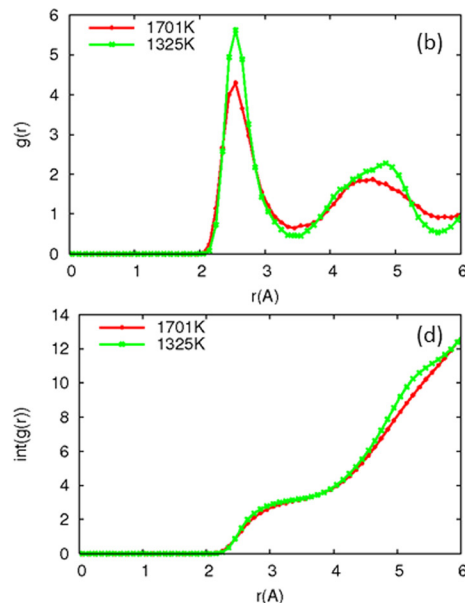


FIG. 27. RDF of Al-Al (a), Ni-Ni (b), Ni-Al (c), and IRDF of Ni-Al (d) for molten 1 Al grain in Ni matrix structure during cooling.

- ¹T. Griffin, S. G. Sundkvist, K. Asen, and T. Bruun, *J. Eng. Gas Turbines Power* **127**, 81 (2005).
- ²R. E. Anderson, S. MacAdam, F. Viteri, D. O. Davies, J. P. Downs, and A. Paluszewski, in ASME Conference Proceedings, Berlin, Germany, GT2008, 9-13 June, 2008.
- ³D. Letzig, J. Klöwer, and G. Sauthoff, *Z. Metallkd.* **90**, 712 (1999).
- ⁴S. C. Deevi and V. K. Sikka, *Intermetallics* **4**, 357 (1996).
- ⁵S. M. Foiles and M. S. Daw, *J. Mater. Res.* **2**, 5 (1987).
- ⁶S. Yu, C.-Y. Wang, T. Yu, and J. Cai, *Physica B* **396**, 138 (2007).
- ⁷M. S. Daw and M. I. Baskes, *Phys. Rev. B* **29**, 6443 (1984).
- ⁸D. Frenkel and B. Smit, *Understanding Molecular Simulation—From Algorithms to Applications*, 2nd ed. (Academic Press, 2002).
- ⁹L. Eunkoo and L. Byeong-Joo, *J. Phys.: Condens. Matter* **22**, 175702 (2010).
- ¹⁰A. O. Mekhrabov and M. V. Akdeniz, *Modell. Simul. Mater. Sci. Eng.* **15**, 1 (2007).
- ¹¹L. Hui, B. Xiufang, and W. Guanghou, *Mater. Sci. Eng. A* **298**, 245 (2001).
- ¹²T. Helander and J. Agren, *Acta Mater.* **47**, 1141 (1999).
- ¹³M. I. Mendelev, A. O. Rodin, and B. S. Bokstein, *Computer Simulation of Diffusion in Dilute Al-Fe Alloys* (Trans Tech Publications Ltd, Lanzarote, Spain, 2009), p. 733.
- ¹⁴M. I. Mendelev, A. O. Rodin, and B. S. Bokstein, *Computer Simulation of Fe Diffusion in Liquid Al and Along Al Grain Boundaries* (Trans Tech Publications Ltd, Moscow, Russia, 2011), p. 223.
- ¹⁵S. B. Debiaggi, P. M. Decorte, and A. M. Monti, *Phys. Status Solidi B* **195**, 37 (1996).
- ¹⁶J. Duan, Y. N. Ossetsky, and D. J. Bacon, *Atomistic Study of Self-Diffusion in Ni, Al and Ni₃Al* (Trans Tech Publications Ltd, Paris, France, 2001), p. 423.
- ¹⁷S. Frank and C. Herzog, *The Effect of Composition and Temperature on Grain Boundary Diffusion of 63Ni in Ni₃Al Alloys* (Elsevier, Switzerland, 1997), p. 882.
- ¹⁸J. Horbach, S. K. Das, A. Griesche, M. P. Macht, G. Frohberg, and A. Meyer, *Phys. Rev. B* **75**, 174304 (2007).
- ¹⁹D. Jinsong, *J. Phys.: Condens. Matter* **19**, 086217 (2007).
- ²⁰W. Li, B. Xiufang, and Z. Jingxiang, *Phys. Chem. Glasses* **43**, 280 (2002).
- ²¹C. Schmidt and J. L. Bocquet, *Calculation of the Diffusion Parameters in an Ordered Ni₃Al-Alloy for a Relaxed Lattice* (Mater. Res. Soc., Warrendale, PA, USA, 1998), p. 165.
- ²²L. Zhang, I. Steinbach, and Y. Du, *Int. J. Mater. Res.* **102**, 371 (2011).
- ²³S. K. Das, J. Horbach, and T. Voigtmann, *Phys. Rev. B* **78**, 064208 (2008).
- ²⁴S. V. Divinski, S. Frank, C. Herzog, and U. Sodervall, *Diffus. Defect Data, Pt. B* **72**, 203 (2000).
- ²⁵A. V. Evteev, E. V. Levchenko, I. V. Belova, and G. E. Murch, *Intermetallics* **19**, 848 (2011).
- ²⁶A. Griesche, B. Zhang, J. Horbach, and A. Meyer, *Atomic Diffusion and Its Relation to Thermodynamic Forces in Al-Ni Melts* (Trans Tech Publications Ltd, Lanzarote, Spain, 2009), p. 705.
- ²⁷Y. Dai, S. Zhu, and F. Wang, *Study on Ni/Al Interface Diffusion at Initial Time by Using Molecular Dynamics Method* (Trans Tech Publications, Shenyang, Liaoning, China, 2012), p. 42.
- ²⁸A. C. T. Van Duin, S. Dasgupta, F. Lorant, and W. A. Goddard III, *J. Phys. Chem. A* **105**, 9396 (2001).
- ²⁹Y. K. Shin, H. Kwak, C. Zou, A. V. Vasenkov, and A. C. T. Van Duin, *J. Phys. Chem. A* **116**, 12163 (2012).
- ³⁰A. Vasenkov, D. Newsome, O. Verners, M. F. Russo, Jr., R. Zaharieva, and A. C. T. Van Duin, *J. Appl. Phys.* **112**, 13511 (2012).
- ³¹M. R. LaBrosse, J. K. Johnson, and A. C. T. van Duin, *J. Phys. Chem. A* **114**, 5855 (2010).
- ³²J. A. Keith, D. Fantauzzi, T. Jacob, and A. C. T. van Duin, *Phys. Rev. B* **81**, 235404 (2010).
- ³³C. Zou, A. C. T. van Duin, and D. Sorescu, *Top. Catal.* **55**, 391 (2012).
- ³⁴J. E. Mueller, A. C. T. van Duin, and W. A. Goddard III, *J. Phys. Chem. C* **114**, 4939 (2010).
- ³⁵K. Chenoweth, A. C. T. van Duin, P. Persson, M. J. Cheng, J. Oxgaard, and W. A. Goddard, *J. Phys. Chem. C* **112**, 14645 (2008).
- ³⁶M. Russo, R. Li, M. Mench, and A. C. T. van Duin, *Int. J. Hydrogen Energy* **36**, 5828 (2011).
- ³⁷J. P. M. Postma, H. J. C. Berendsen, W. F. van Gunsteren, A. DiNola, and J. R. Haak, *J. Chem. Phys.* **81**, 3684 (1984).
- ³⁸*LAMMPS Users Manual*, Vol. 2013, available from <http://lammps.sandia.gov>.
- ³⁹G. Wulff, *Z. Kristallogr.* **34**, 449 (1901).
- ⁴⁰L. D. Marks, *Surf. Sci.* **150**, 358 (1985).
- ⁴¹Y. Saito, *J. Cryst. Growth* **53**, 273 (1981).
- ⁴²M. Friak and J. Neugebauer, *Ab Initio Study of the Anomalous Volume-Composition Dependence in Fe-Al Alloys* (Elsevier Ltd, Oxford, UK, 2010), p. 1316.
- ⁴³Y. Wang, Z. K. Liu, and L. Q. Chen, *Acta Mater.* **52**, 2665 (2004).
- ⁴⁴M. Zhou, *Theoretical Interpretation of the Virial Stress* (American Institute of Aeronautics and Astronautics Inc., Norfolk, VA, USA, 2003), p. 3368.
- ⁴⁵H. B. Liu, K. Y. Chen, G. Y. An, and Z. Q. Hu, *Philos. Mag. B* **76**, 75 (1997).
- ⁴⁶H. Assadi and A. L. Greer, *ISIJ Int.* **35**, 574 (1995).
- ⁴⁷P. R. Swann, W. R. Duff, and R. M. Fisher, *Mat. Trans.* **3**, 409 (1972).
- ⁴⁸G. W. C. Kaye and T. H. Laby, *Tables of Physical and Chemical Constants*, 15th ed. (Longman, London, 1993).
- ⁴⁹A. M. James and M. P. Lord, *Macmillan's Chemical and Physical Data* (Macmillan, London, 1992).
- ⁵⁰W. Witt, *Z. Naturforsch. A* **22A**, 92 (1967).
- ⁵¹J. Budzien, A. P. Thompson, and S. V. Zybin, *J. Phys. Chem. B* **113**, 13142 (2009).
- ⁵²M. C. Pitman and A. C. T. Van Duin, *J. Am. Chem. Soc.* **134**, 3042 (2012).